Research Article

Ming-Cui Li*, Ai-Xi Chen, and Wei Zeng

Tripartite entanglement and entanglement transfer in a hybrid cavity magnomechanical system

https://doi.org/10.1515/phys-2022-0240
received October 25, 2022; accepted March 15, 2023

Abstract: We propose to realize bipartite and tripartite entanglements transfer in a cavity magnomechanical system consisting of a microwave cavity with an yttrium iron garnet (YIG) sphere and a silicon-nitride membrane in it. The initial magnon–YIG phonon entanglement and photon-membrane phonon entanglement caused by the magnetostrictive interaction and the optomechanical interaction can be effectively transferred to magnon–membrane phonon entanglement and photon–YIG phonon entanglement. Photon–magnon–YIG phonon and photon–magnon–membrane phonon entanglements can also be realized in the system. These two types of tripartite entanglements can be easily transferred from one type to the other by adjusting the detuning or dissipation ratio. Moreover, the bipartite and tripartite entanglements and their transfer are all robust against temperature. Furthermore, by introducing supermodes formed by the photon and magnon modes, we find that the entanglement between the two mechanical modes can be obtained under the condition of an extremely low temperature. And the effective detuning region of the YIG phonon-membrane phonon entanglement is complementary to the detuning regions of other bipartite entanglements. Our results indicate that the combination of cavity magnomechanical and optomechanical systems could provide more flexible controllability of bipartite and tripartite entanglements and their transfer and could serve as a potential quantum interface among microwave, magnon, and mechanical systems.

Keywords: tripartite entanglement, transfer, magnon, cavity

*** Corresponding author: Ming-Cui Li,** School of Information Engineering, East China Jiaotong University, Nanchang 330013, China, e-mail: cacaony@163.com
Ai-Xi Chen: School of Science, Zhejiang Sci-Tech University, Hangzhou 310018, China
Wei Zeng: School of Information Engineering, East China Jiaotong University, Nanchang 330013, China

1 Introduction

Magnons, the quanta of spin waves, can be used in the novel wave-based computing technologies with the advantages of low dissipation of energy, much smaller footprints [1,2], *etc*. With very high spin density and uniquely low magnetic damping, yttrium iron garnet (YIG) becomes a promising magnon system candidate for quantum information processing [2,3]. In the quantum regime, strong coupling of the Kittle mode in a YIG sphere to a microwave mode has been achieved both at cryogenic and room temperatures [4–6], and ultrastrong coupling is also demonstrated [7]. Furthermore, coherent *in situ* control on the magnon–photon coupling [8], and indirect coupling between the separated cavity mode and magnon mode [9] are put forward. By analogy with cavity optomechanics [10], cavity magnomechanics is reported, where the phonon–magnon interaction resulting from the magnetostrictive forces is studied [11]. The magnon Kerr effect as a result of the magnetocrystalline anisotropy in YIG is experimentally demonstrated and theoretically analyzed in a cavity–magnon system [12,13]. The hybrid cavity–magnon system provides more controllable degrees of freedom and helps us investigate various properties of the compound system, such as magnon-polariton bistability [14], magnon-induced nonreciprocity [15], magnon blockade due to qubit–magnon coupling [16,17], photon–phonon–magnon simultaneous blockade effect [18], magnon blockade in a parity-time-symmetric-like cavity magnomechanical system [19], sub-Poissonian statistics of magnons resulting from Kerr effect [20], *etc*.

Entanglement [21] is considered to be a crucial resource for quantum communication and information processing. Entanglement can be achieved in many systems, such as entanglement between a cavity mode and a movable mirror [22], between an exciton and a mechanical mode [23], between two mechanical oscillators [24], and so on. The cavity–magnon system provides a good platform for the study of entanglement among optical modes,

magnon modes, mechanical modes, atoms, *etc*. Entanglements between magnon modes, between magnon mode and photon mode, can be generated *via* activating Kerr nonlinear effect [25,26]. With the help of the squeezed microwave field generated by the parametric amplifier [27], or the help of or an artificial atom [28], effective entanglement between magnon modes can also be generated. It is also found that based on the magnetic dipole interaction and the magnetostrictive interaction, the magnon–photon–phonon tripartite entanglement can be achieved [29]. Entanglement transfer [30–32] among various modes means that one entanglement tends to decrease while the other tends to increase. The purpose of entanglement transfer is to achieve the transfer of source entanglement to target entanglement or near-entanglement to long-range entanglement. The scheme to realize the perfect transfer between different entanglements in a parity-time-symmetric-like cavity magnomechanical system was proposed in 2021 [33].

A hybrid cavity–magnon system can contain many different modes, such as photon modes, magnon modes, phonon modes, and atoms, simultaneously, which provides a good platform for the hybrid quantum information processing system with magnon as the medium [34]. Based on a hybrid cavity–magnon system, we try to find bipartite and tripartite entanglements between different modes. We focus on the entanglements between the modes without direct interactions and analyze the underlying physical mechanism of the creation of entanglements and entanglement transfer in the system.

2 The model

The system considered in this article is shown in Figure 1. In a hybrid cavity–magnomechanical system, a YIG sphere and a mechanical membrane are located in a microwave cavity. The frequency of the magnon mode in the YIG sphere can be tuned by an external bias magnetic field B_0, *i.e.*, $\omega_m = \tilde{\gamma}B_0$, where $\tilde{\gamma}$ is the gyromagnetic ratio. The YIG sphere also supports phonon mode resulting from the geometry deformation of the YIG sphere, which is induced by the magnon excitation. We consider a microwave field that drives the YIG sphere directly, and the driving magnetic field, the bias magnetic field, and the magnetic field of cavity mode are perpendicular to each other at the site of the YIG sphere. Three kinds of direct couplings exist in this system, the photon–magnon coupling resulting from the magnetic dipole interaction between the cavity mode and the magnon mode, the magnon–YIG phonon coupling induced by the magnetostrictive interaction in the YIG

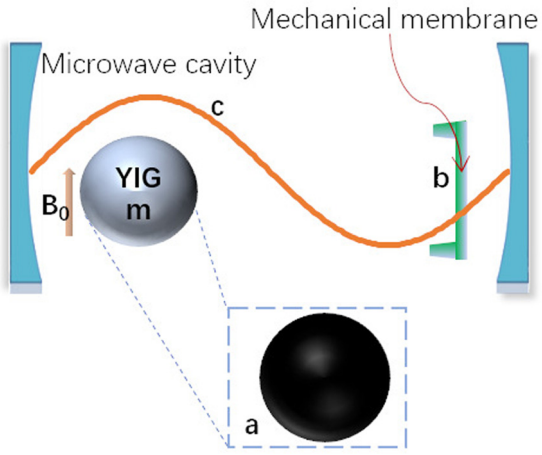

Figure 1: Schematic diagram of the system. A YIG sphere and a mechanical membrane are placed inside a microwave cavity. The YIG sphere is magnetized by a bias magnetic field B_0. The cavity photons are coupled to the magnons in the YIG sphere *via* magnetic dipole interaction, and to the phonons in the mechanical membrane *via* optomechanical interaction. There also exists magnon-phonon coupling induced by magnetostrictive interaction in the YIG sphere.

sphere, and the photon–membrane phonon coupling *via* optomechanical interaction. The Hamiltonian of the system H consists of free Hamiltonian H_0, interaction Hamiltonian $H_{\rm int}$, and Hamiltonian $H_{\rm d}$ describing the external driving of the magnon mode as follows:

$$H/\hbar = H_0 + H_{\rm int} + H_{\rm d}. \tag{1}$$

$$H_0 = \omega_{\rm c} c^\dagger c + \omega_{\rm m} m^\dagger m + \frac{\omega_{\rm a}}{2}(q_{\rm a}^2 + p_{\rm a}^2) + \frac{\omega_{\rm b}}{2}(q_{\rm b}^2 + p_{\rm b}^2). \tag{2}$$

$$H_{\rm int} = g_{\rm om}(cm^\dagger + c^\dagger m) + g_{\rm ma} m^\dagger m q_{\rm a} + g_{\rm ob} c^\dagger c q_{\rm b}. \tag{3}$$

$$H_{\rm d} = i\Omega_{\rm m}\left(e^{-iw_{\rm d}t}m^\dagger - e^{iw_{\rm d}t}m\right). \tag{4}$$

Here, $c^\dagger$ (c) and $m^\dagger$ (m) are the creation (annihilation) operators of the cavity mode (at frequency $\omega_{\rm c}$) and the magnon mode (at frequency $\omega_{\rm m}$). $q_{\rm a}$ ($p_{\rm a}$) and $q_{\rm b}$ ($p_{\rm b}$) are the dimensionless position (momentum) operators of the YIG mechanical mode (at frequency $\omega_{\rm a}$) and the membrane mechanical mode (at frequency $\omega_{\rm b}$). These operators satisfy the commutation relations $[c, c^\dagger] = 1$, $[m, m^\dagger] = 1$, $[q_{\rm a}, p_{\rm a}] = i$, and $[q_{\rm b}, p_{\rm b}] = i$. $g_{\rm om}$, $g_{\rm ma}$, and $g_{\rm ob}$ are the photon–magnon coupling rate, single-magnon magnomechanical coupling rate, and single-photon optomechanical coupling rate, respectively. Eq. (4) denotes the magnon mode that is driven by a microwave field at frequency $\omega_{\rm d}$ with driving strength $\Omega_{\rm m}$.

In the frame rotating with $\tilde{H}_0/\hbar = \omega_{\rm d} c^\dagger c + \omega_{\rm d} m^\dagger m$, the Langevin equations describing the dynamics of the system are given as follows:

$$\begin{aligned}
\dot{c} &= -[\kappa_c + i(\Delta_c + g_{ob}q_b)]c - ig_{om}m + \sqrt{2\kappa_c}c_{in},\\
\dot{m} &= -[\kappa_m + i(\Delta_m + g_{ma}q_a)]m - ig_{om}c + \Omega_m\\
&\quad + \sqrt{2\kappa_m}m_{in},\\
\dot{q}_a &= \omega_a p_a,\\
\dot{p}_a &= -\omega_a q_a - \gamma_a p_a - g_{ma}m^\dagger m + \xi_a,\\
\dot{q}_b &= \omega_b p_b,\\
\dot{p}_b &= -\omega_b q_b - \gamma_b p_b - g_{ob}c^\dagger c + \xi_b,
\end{aligned} \tag{5}$$

where k_c and κ_m are dissipation rates of the cavity and magnon modes, γ_a and γ_b are the damping rates of the YIG mechanical mode, and membrane mechanical mode, $\Delta_c = \omega_c - \omega_d$, and $\Delta_m = \omega_m - \omega_d$. c_{in}, m_{in}, ξ_a, and ξ_b, which all have zero mean values, are the input noise operators for the cavity mode, magnon mode, YIG mechanical mode and membrane mechanical mode. Assuming each mechanical mode in the system is with good quality factor, the non-zero correlation functions of the input noise operators are

$$\begin{aligned}
\langle I_{in}(t)I_{in}^\dagger(t')\rangle &= [n_I(\omega_I) + 1]\delta(t - t'),\\
\langle I_{in}^\dagger(t)I_{in}(t')\rangle &= n_I(\omega_I)\delta(t - t'),
\end{aligned} \tag{6}$$

$$\langle \xi_J(t)\xi_J(t') + \xi_J(t')\xi_J(t)\rangle/2 \simeq \gamma_J[2n_J(\omega_J) + 1]\delta(t - t'), \tag{7}$$

where $I = \{c, m\}$, $J = \{a, b\}$, and $n_S(\omega_S) = [\exp(\frac{\hbar\omega_S}{K_B T}) - 1]^{-1}$ ($S = I, J$) are the equilibrium mean thermal photon, magnon, and phonon number.

In the strongly driving regime, the Langevin equations in Eq. (5) can be linearized by decomposing each operator as the sum of its steady-state value and a small fluctuation, *i.e.*, $O = O_s + \delta O$ ($O = c, m, q_a, p_a, q_b, p_b$). The steady-state values of the operators can be obtained by setting Eq. (5) to zero and calculating from the algebraic equations. The linearized Langevin equations are given as follows:

$$\begin{aligned}
\delta\dot{c} &= -(\kappa_c + i\Delta_c)\delta c - ig_{om}\delta m - ig_{ob}q_{bs}\delta c - ig_{ob}c_s\delta q_b\\
&\quad + \sqrt{2\kappa_c}c_{in},
\end{aligned} \tag{8}$$

$$\begin{aligned}
\delta\dot{m} &= -(\kappa_m + i\Delta_m)\delta m - ig_{ma}q_{as}\delta m - ig_{ma}m_s\delta q_a\\
&\quad - ig_{om}\delta c + \sqrt{2\kappa_m}m_{in},
\end{aligned} \tag{9}$$

$$\delta\dot{q}_a = \omega_a\delta p_a, \tag{10}$$

$$\delta\dot{p}_a = -\gamma_a\delta p_a - \omega_a\delta q_a - g_{ma}m_s\delta m^\dagger - g_{ma}m_s^*\delta m + \xi_a, \tag{11}$$

$$\delta\dot{q}_b = \omega_b\delta p_b, \tag{12}$$

$$\delta\dot{p}_b = -\gamma_b\delta p_b - \omega_b\delta q_b - g_{ob}c_s\delta c^\dagger - g_{ob}c_s^*\delta c + \xi_b. \tag{13}$$

The steady-state entanglement in the system can be analyzed from the dynamics of the quadrature fluctuations of the operators, which are defined as follows: $\delta X_I = (\delta I^\dagger + \delta I)/\sqrt{2}$, $\delta Y_I = i(\delta I^\dagger - \delta I)/\sqrt{2}$, $X_{Iin} = (I_{in}^\dagger + I_{in})/\sqrt{2}$, $Y_{Iin} = i(I_{in}^\dagger - I_{in})/\sqrt{2}$, $I = \{c, m\}$. Eqs. (8)–(13) can be rewritten as $\dot{U}(t) = AU(t) + N(t)$, where $U^T = (\delta X_c, \delta Y_c, \delta X_m, \delta Y_m, \delta q_a, \delta p_a, \delta q_b, \delta p_b)$, $N^T = (\sqrt{2\kappa_c}X_{cin}, \sqrt{2\kappa_c}Y_{cin}, \sqrt{2\kappa_m}X_{min}, \sqrt{2\kappa_m}Y_{min}, 0, \xi_a, 0, \xi_b)$, and the drift matrix A is given by Eq. (14).

$$A = \begin{bmatrix}
-\kappa_c & \Delta_c + g_{ob}q_{bs} & 0 & g_{om} & 0 & 0 & \sqrt{2}g_{ob}\mathrm{Im}(c_s) & 0\\
-(\Delta_c + g_{ob}q_{bs}) & -\kappa_c & -g_{om} & 0 & 0 & 0 & -\sqrt{2}g_{ob}\mathrm{Re}(c_s) & 0\\
0 & g_{om} & -\kappa_m & \Delta_m + g_{ma}q_{as} & \sqrt{2}g_{ma}\mathrm{Im}(m_s) & 0 & 0 & 0\\
-g_{om} & 0 & -(\Delta_m + g_{ma}q_{as}) & -\kappa_m & -\sqrt{2}g_{ma}\mathrm{Re}(m_s) & 0 & 0 & 0\\
0 & 0 & 0 & 0 & 0 & \omega_a & 0 & 0\\
0 & 0 & -\sqrt{2}g_{ma}\mathrm{Re}(m_s) & -\sqrt{2}g_{ma}\mathrm{Im}(m_s) & -\omega_a & -\gamma_a & 0 & 0\\
0 & 0 & 0 & 0 & 0 & 0 & 0 & \omega_b\\
-\sqrt{2}g_{ob}\mathrm{Re}(c_s) & -\sqrt{2}g_{ob}\mathrm{Im}(c_s) & 0 & 0 & 0 & 0 & -\omega_b & -\gamma_b
\end{bmatrix} \tag{14}$$

On the condition of the Gaussian property of the input noises and the linearized Langevin equations, the steady state of the quantum fluctuations in the system is a Gaussian state and fully characterized by a 8×8 covariance matrix V with $V_{ij} = \langle U_i(\infty)U_j(\infty) + U_j(\infty)U_i(\infty)\rangle/2$. When the system is stable, the covariance matrix V satisfies the Lyapunov equation $AV + VA^T = -D$ [22]. The elements of matrix D are obtained using the correlations of the noise operators, $D_{ij}\delta(t - t') = \langle N_i(t)N_j(t') + N_j(t')N_i(t)\rangle/2$. Here, $D = \mathrm{diag}[\kappa_c(2n_c + 1), \kappa_c(2n_c + 1), \kappa_m(2n_m + 1), \kappa_m(2n_m + 1), 0, \gamma_a(2n_a + 1), 0, \gamma_b(2n_b + 1)]$.

We adopt the logarithmic negativity [35,36] EN to measure the bipartite entanglement of the system, which is given as follows:

$$EN = \max[0, -\ln 2\upsilon_-]. \tag{15}$$

Here, $\upsilon_- = \min\mathrm{eig}|i\varsigma_2\tilde{v}_4|$, $\varsigma_2 = \oplus_{j=1}^2 i\sigma_y$, σ_y is the y-Pauli matrix, $\tilde{v}_4 = \mathrm{P}_{1|2}v_4\mathrm{P}_{1|2}$, v_4 is the 4×4 submatrix related only to the two target modes, and the matrix $\mathrm{P}_{1|2} = \mathrm{diag}\{1, -1, 1, 1\}$.

The residual contangle is adopted to investigate tripartite entanglement of the system. The quantification of tripartite entanglement is given by the minimum residual contangle [22,37].

$$\begin{aligned}
\Re_\tau^{\min cab} &= \min[\Re_\tau^{c|ab}, \Re_\tau^{a|cb}, \Re_\tau^{b|ca}],\\
\Re_\tau^{\min mab} &= \min[\Re_\tau^{m|ab}, \Re_\tau^{a|mb}, \Re_\tau^{b|ma}],\\
\Re_\tau^{\min cma} &= \min[\Re_\tau^{c|ma}, \Re_\tau^{m|ca}, \Re_\tau^{a|cm}],\\
\Re_\tau^{\min cmb} &= \min[\Re_\tau^{c|mb}, \Re_\tau^{m|cb}, \Re_\tau^{b|cm}],
\end{aligned} \tag{16}$$

where $\Re_\tau^{\min}$ is a genuine three-way property of any three-mode Gaussian state [29], $\Re_\tau^{i|jk} \equiv C_{i|jk} - C_{i|j} - C_{i|k} \geq 0$ ($i, j, k = c, m, a, b$) with $C_{u|v}$ (v contains one or two modes) the squared logarithmic negativity.

3 Bipartite and tripartite entanglements in the system

Based on the experimental reachable parameters [10,11,29,33], we plot the bipartite entanglements *versus* detuning Δ_m in Figure 2(a)–(f). The stability of the system is guaranteed by numerically calculating the eigenvalues of the drift matrix A. When the real parts of all the eigenvalues of matrix A are negative, the system is stable. Here, EN_{cb} denotes the photon–membrane phonon entanglement, EN_{ma} the magnon–YIG phonon entanglement, and EN_{mb} the magnon–membrane phonon entanglement. The entanglements between the photon mode and the magnon mode EN_{cm}, between the membrane phonon and the YIG phonon mode EN_{ab}, between the photon mode and the YIG phonon mode EN_{ca} are almost zero with the parameters given in Figure 2. As shown in Figure 2(a), when the coupling strength (g_{om}) between the cavity mode and the magnon mode is small (smaller than the magnon dissipation rates κ_m and the cavity dissipation rate κ_c), entanglement only appears in the magnon–YIG phonon subsystem, which is due to the direct nonlinear magnetostrictive interaction in the magnon–YIG phonon subsystem. In Figure 2(b), g_{om} rises to the same order of magnitude of κ_m and $g_{om} > \kappa_m, \kappa_c$, entanglements appear both in the photon–membrane subsystem and magnon–YIG phonon subsystem. The photon number in the cavity is enhanced by the beam-splitter interaction between the photon mode and the magnon mode, which is shown in the first term in Eq. (3), and then the direct nonlinearity optomechanical interaction is used to generate the entanglement between the photon mode and the membrane phonon mode. With the increase of the photon–magnon coupling rate, g_{om}, the entanglement, EN_{mb} in the magnon–membrane subsystem appears and increases gradually. Meanwhile, EN_{ma} decreases gradually, which means the initial entanglement in the magnon–YIG phonon subsystem partially transfers to the magnon–membrane subsystem in which no direct interaction exists. When g_{om} increases to $2\omega_a$, the initial entanglement in the magnon–YIG phonon subsystem is transferred totally to the magnon–membrane subsystem, and one can switch the entanglement in cavity-membrane subsystem to the entanglement in magnon–membrane subsystem by tuning Δ_m, as shown in Figure 2(f).

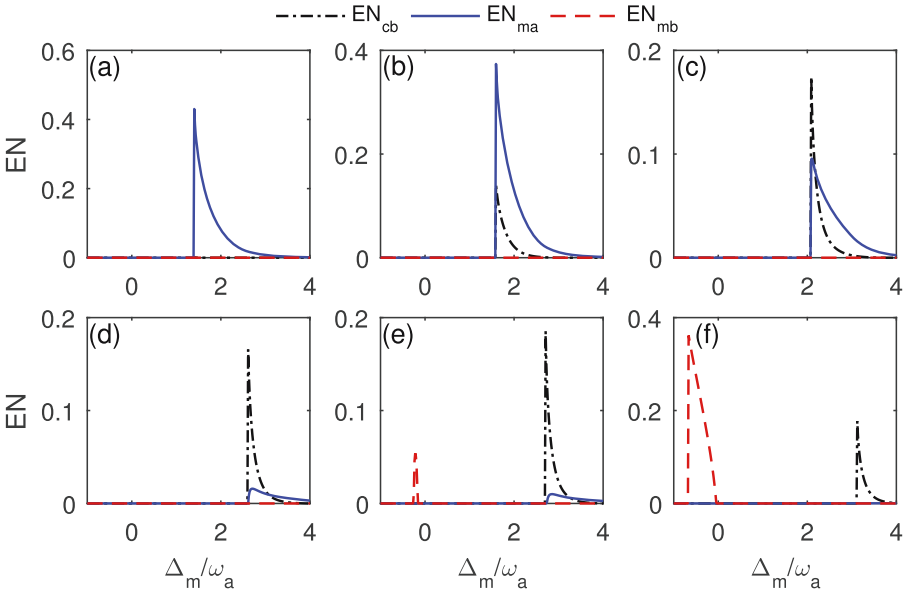

Figure 2: Bipartite entanglements EN_{cb}, EN_{ma}, EN_{mb} *versus* detuning Δ_m with (a) $g_{om} = 0.05\omega_a$, (b) $g_{om} = 0.5\omega_a$, (c) $g_{om} = \omega_a$, (d) $g_{om} = 1.5\omega_a$, (e) $g_{om} = 1.6\omega_a$, (f) $g_{om} = 2\omega_a$. Other parameters are: $\Delta_c = \Delta_m$, $\omega_d/2\pi = 9$ GHz, $\kappa_c/2\pi = \kappa_m/2\pi = 1$ MHz, $\omega_a/2\pi = \omega_b/2\pi = 10$ MHz, $\gamma_a = \gamma_b = 100$ Hz, $g_{ma}/2\pi = 0.4$ Hz, $g_{ob} = 2g_{ma}$, $P = 17.5$ mW, $T = 10$ mK.

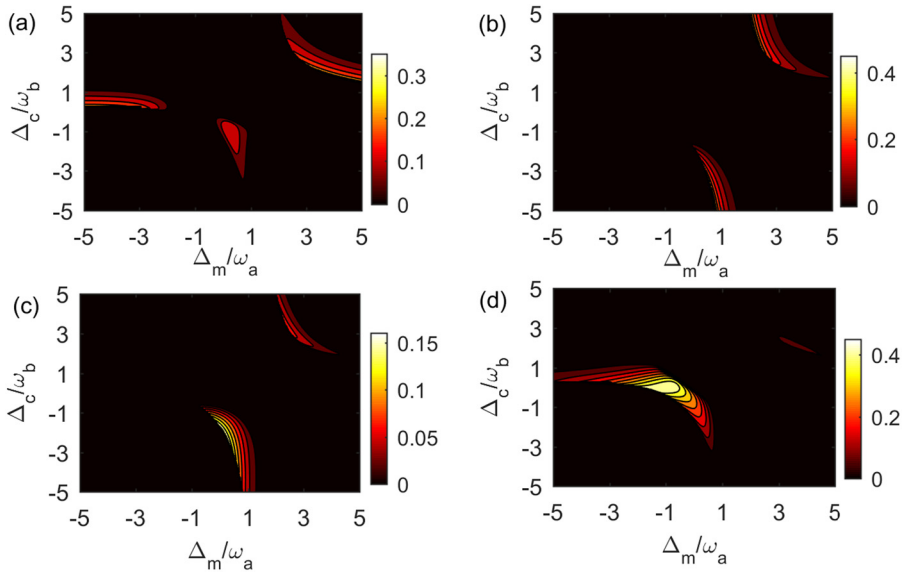

Figure 3: Plot of bipartite entanglement (a) EN_{cb}, (b) EN_{ma}, (c) EN_{ca}, (d) EN_{mb} *versus* detunings Δ_m and Δ_c. The other parameters are the same as in Figure 2(f) except for $\omega_b = 1.3\omega_a$.

To find the optimal detunings for different bipartite entanglements, in Figure 3, we show the bipartite entanglements *versus* Δ_m and Δ_c. The frequencies of the two mechanical oscillators are set to be different, which is helpful to analyze the entanglements in different subsystems. Weak entanglement between the photon mode and the magnon mode exists; however EN_{cm} is too small and not shown here. The entanglement between the two mechanical oscillators is almost 0. The effective entanglements EN_{cb} and EN_{ma} are mainly located in the regions of $\Delta_c > 0$ and $\Delta_m > 0$, respectively. As shown in Figure 3(b), the two effective entanglement regions of EN_{ma} are as follows: $\Delta_m \approx \omega_a$ and $\Delta_c < 0$, $\Delta_m \approx 2\omega_a$ and $\Delta_c > 0$. The two main effective entanglement regions of EN_{cb} are as follows: $\Delta_c \approx \omega_b$ and $\Delta_m < 0$, $\Delta_c \approx 2\omega_b$ and $\Delta_m > 0$, as shown in Figure 3(a). In the first effective region of magnon–YIG phonon entanglement, the magnetostrictive interaction significantly cools the YIG mechanical mode and the entanglement between these two modes is generated due to the nonlinear coupling. Similarly, in the first effective entanglement region of photon–membrane phonon subsystem, the optomechanical interaction cools the membrane mechanical mode, and the entanglement is simultaneously generated. In the region $\Delta_c > 0$ and $\Delta_m > 0$, due to the side-band cooling effects of the magnetostrictive interaction and the optomechanical interaction, this region is favorable for both EN_{ma} and EN_{cb}. Since both the YIG mechanical mode and the membrane mechanical mode need to be cooled, in this region, the optimal detuning for EN_{ma} shifts to $\Delta_m \approx 2\omega_a$, and the optimal detuning for EN_{cb} shifts to $\Delta_c \approx 2\omega_b$. When $\Delta_c < 0$, the optomechanical interaction will heat the membrane mechanical oscillator, which will destroy the initial entanglement between the photon mode and the membrane phonon mode. Similarly, the initial magnon–YIG phonon entanglement will be destroyed if $\Delta_m < 0$ due to the heating of YIG mechanical mode. In these regions, effective cross entanglements in photon-YIG phonon subsystem and magnon–membrane phonon subsystem are obtained instead, as shown in Figure 3(c) and (d). Especially, the maximum value of EN_{mb} locates at $\Delta_m \approx -\omega_a$, where the magnon mode is resonant with the red sideband ($\omega_m = \omega_d - \omega_a$). At this detuning, the initial magnon–YIG phonon entanglement transfers totally to the magnon–membrane phonon entanglement, *i.e.*, EN_{ma} disappears totally and EN_{mb} reaches its maximum value. This means the local entanglement in magnon–YIG phonon subsystem arising from the initial nonlinear coupling can be transferred to distant entanglement between the magnon mode and the membrane phonon mode *via* tuning Δ_m and Δ_c.

As shown in Figure 4, effective tripartite entanglements exist in the cavity–magnon–YIG phonon subsystem and the cavity–magnon–membrane phonon subsystem. Figure 4(a) and (b) show that, when the two mechanical modes are of the same frequency (*i.e.*, $\omega_a = \omega_b$) and the cavity mode resonates with the magnon mode ($\Delta_c = \Delta_m$), one can switch tripartite entanglement between cavity–magnon–YIG phonon subsystem and cavity–magnon–membrane phonon subsystem by adjusting g_{ob} and κ_m. As shown in Figure 4(a), when the optomechanical

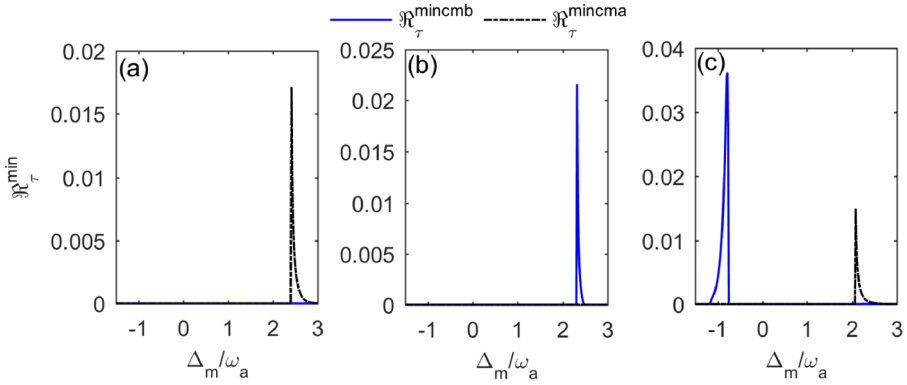

Figure 4: Minimum residual contangle $\Re_\tau^{\mathrm{min}}$ *versus* detuning Δ_m with $g_{ob} = g_{ma}$, $\kappa_m = 0.1\kappa_c$, $\omega_b = \omega_a$, $\Delta_c = \Delta_m$ in (a), $g_{ob} = 2g_{ma}$, $\kappa_m = 11\kappa_c$, $\omega_b = \omega_a$, $\Delta_c = \Delta_m$ in (b) and $g_{ob} = g_{ma}$, $\kappa_m = 0.1\kappa_c$, $\omega_b = 1.3\omega_a$, $\Delta_c = \Delta_m + \omega_b$ in (c). Other parameters are the same as in Figure 2 except for $g_{om} = 1.5\omega_a$.

coupling strength g_{ob} equals the magnomechanical coupling strength g_{ma} and the dissipation rate of the magnon mode κ_m is smaller than that of the cavity mode κ_c, the tripartite entanglement mainly exists in the cavity–magnon–YIG phonon subsystem due to the direct driving of magnon mode. In Figure 4(b), because g_{ob} is larger than g_{ma}, and $\kappa_m > \kappa_c$, the number of photons obtained by the magnon-photon beam splitter interaction is increased, the entanglement EN_{cb} and the indirect interaction between magnon mode and membrane phonon mode are thus enhanced. Therefore, the tripartite entanglement mainly exists in the cavity–magnon–membrane phonon subsystem. In Figure 4(c), the conditions, $g_{ob} = g_{ma}$ and $\kappa_m < \kappa_c$, facilitate us to obtain the tripartite entanglement in the cavity–magnon–YIG phonon subsystem. Interestingly, at the same time, we distinguish the frequencies of the YIG mechanical mode and the membrane mechanical mode, and make $\Delta_c = \Delta_m + \omega_b$ (*i.e.*, $\omega_c - \omega_m = \omega_b$), which will lead to the interaction effect of $c^\dagger mb + cm^\dagger b^\dagger$, and thus, the tripartite entanglement in the cavity–magnon–membrane phonon subsystem is enhanced. Therefore, as shown in Figure 4(c), one can obtain tripartite entanglements both in the cavity–magnon–YIG phonon subsystem and cavity–magnon–membrane phonon subsystem, which can be easily switched by adjusting the detuning Δ_m.

4 Calculating with supermodes

To further analyze the entanglements in the strong photon–magnon coupling regime and explore the entanglement between the YIG phonon mode and the membrane phonon mode, we introduce two supermodes $\varphi_\pm = (c \pm m)/\sqrt{2}$ [38], which are the maximum hybridized modes between the photon and magnon modes. Assuming the cavity mode resonates with the magnon mode, *i.e.*, $\Delta = \Delta_c = \Delta_m$, the Hamiltonian in Eq. (1) to (4) is rewritten as follows:

$$H_0' = (\Delta + g_{om})\varphi_+^\dagger\varphi_+ + (\Delta - g_{om})\varphi_-^\dagger\varphi_- + \omega_a a^\dagger a + \omega_b b^\dagger b, \tag{17}$$

$$H_{\mathrm{int}}' = \eta_a(\varphi_+^\dagger\varphi_+ + \varphi_-^\dagger\varphi_- - \varphi_+^\dagger\varphi_- - \varphi_+\varphi_-^\dagger)(a^\dagger + a)/\sqrt{2} + \eta_b(\varphi_+^\dagger\varphi_+ + \varphi_-^\dagger\varphi_- + \varphi_+^\dagger\varphi_- + \varphi_+\varphi_-^\dagger)(b^\dagger + b)/\sqrt{2}, \tag{18}$$

$$H_d' = i\Omega_m(\varphi_+^\dagger - \varphi_+ - \varphi_-^\dagger + \varphi_-)/\sqrt{2}, \tag{19}$$

where $\eta_a = g_{ma}/2$, $\eta_b = g_{ob}/2$, $a^\dagger$ (a) and $b^\dagger$ (b) are the creation (annihilation) operators of the YIG phonon mode and the membrane phonon mode, $(a^\dagger + a)/\sqrt{2} = q_a$, $i(a^\dagger - a)/\sqrt{2} = p_a$, $(b^\dagger + b)/\sqrt{2} = q_b$, and $i(b^\dagger - b)/\sqrt{2} = p_b$. In the frame rotating with H_0', choosing $\omega_a = \omega_b = 2g_{om}$ and applying the rotating-wave approximation, we obtain the effect interaction Hamiltonian $\tilde{H}_{\mathrm{int}}$

$$\tilde{H}_{\mathrm{int}} = -\eta_a\varphi_+^\dagger\varphi_- a/\sqrt{2} - \eta_a\varphi_+\varphi_-^\dagger a^\dagger/\sqrt{2} + \eta_b\varphi_+^\dagger\varphi_- b/\sqrt{2} + \eta_b\varphi_+\varphi_-^\dagger b^\dagger/\sqrt{2}. \tag{20}$$

The interaction Hamiltonian reads a parametric down-conversion interaction, that is, one excitation in supermode φ_+ will be accompanied by one annihilation in supermode φ_- and one annihilation in YIG mechanical mode (or membrane mechanical mode). The interaction between supermode φ_- and phonon mode a (b) describes a parametric-type interaction which can generate the entanglement between supermode φ_- and phonon mode a (b). The Langevin equations reads as follows:

$$\dot{\varphi}_{+} = -[i(\Delta + g_{om}) + \gamma]\varphi_{+} + i\eta_a\varphi_{-}a/\sqrt{2} - i\eta_b\varphi_{-}b/\sqrt{2} + \Omega_m/\sqrt{2} + \sqrt{2\gamma}\varphi_{+in}, \quad (21)$$

$$\dot{\varphi}_{-} = -[i(\Delta - g_{om}) + \gamma]\varphi_{-} + i\eta_a\varphi_{+}a^{\dagger}/\sqrt{2} - i\eta_b\varphi_{+}b^{\dagger}/\sqrt{2} - \Omega_m/\sqrt{2} + \sqrt{2\gamma}\varphi_{-in}, \quad (22)$$

$$\dot{a} = -(i\omega_a + \gamma_a)a + i\eta_a\varphi_{+}\varphi_{-}^{\dagger}/\sqrt{2} + \sqrt{2\gamma_a}a_{in}, \quad (23)$$

$$\dot{b} = -(i\omega_b + \gamma_b)b - i\eta_b\varphi_{+}\varphi_{-}^{\dagger}/\sqrt{2} + \sqrt{2\gamma_b}b_{in}, \quad (24)$$

where $\gamma = (\kappa_c + \kappa_m)/2$, $\varphi_{+in} = (c_{in} + m_{in})/\sqrt{2}$, $\varphi_{-in} = (c_{in} - m_{in})/\sqrt{2}$. Similar to Section 2, the Langevin equations in Eqs. (21)–(24) can be linearized and then rewritten using corresponding quadrature operators as $\dot{\tilde{U}}(t) = \tilde{A}\tilde{U}(t) + \tilde{N}(t)$ with $\tilde{U}^{T} = (\delta X_{\varphi+}, \delta Y_{\varphi+}, \delta X_{\varphi-}, \delta Y_{\varphi-}, \delta X_a, \delta Y_a, \delta X_b, \delta Y_b)$, and $\tilde{N}^{T} = (\sqrt{2\gamma}X_{\varphi+in}, \sqrt{2\gamma}Y_{\varphi+in}, \sqrt{2\gamma}X_{\varphi-in}, \sqrt{2\gamma}Y_{\varphi-in}, \sqrt{2\gamma_a}X_{ain}, \sqrt{2\gamma_a}Y_{ain}, \sqrt{2\gamma_b}X_{bin}, \sqrt{2\gamma_b}Y_{bin})$. The drift matrix $\tilde{A}$ is given by Eq. (25), where $\tilde{\eta}_a = \eta_a/\sqrt{2}$, and $\tilde{\eta}_b = \eta_b/\sqrt{2}$.

since the interaction between YIG mechanical mode a and the supermode φ_{-} is the same as that between the membrane mechanical mode b and the supermode φ_{-}, the entanglement between φ_{-} and a is almost the same as that between φ_{-} and b, and the two entanglement curves EN_{s2a} and EN_{s2b} are completely coincident. When $g_{ob} > g_{ma}$, EN_{s2b} is obviously stronger than EN_{s2a}, as shown in Figure 5(c)–(f). Interestingly, entanglement also appears between the two mechanical modes a and b without direct interaction. Figure 5(c)–(f) shows that when $g_{ob} > g_{ma}$, the increase and decrease of EN_{ab} are almost opposite to those in other subsystems. Entanglements in other subsystems transfer to YIG phonon-membrane phonon subsystem within a specific detuning range. Taking Figure 5(c) as an example, as the detuning Δ increases from $0.5\omega_a$ to $1.3\omega_a$, the bipartite entanglements EN_{s2a}, EN_{s2b}, and EN_{s1s2} disappear gradually, while the entanglement EN_{ab} increases gradually. When Δ exceeds $1.3\omega_a$, the entanglement EN_{ab} drops sharply to 0, and the

$$\tilde{A} = \begin{bmatrix} -\gamma & \Delta + g_{om} & \tilde{\eta}_b\mathrm{Im}(b_s) - \tilde{\eta}_a\mathrm{Im}(a_s) \\ -(\Delta + g\mathrm{om}) & -\gamma & \tilde{\eta}_b\mathrm{Re}(a_s) - \tilde{\eta}_a\mathrm{Re}(b_s) \\ \tilde{\eta}_a\mathrm{Im}(a_s) - \tilde{\eta}_b\mathrm{Im}(b_s) & \tilde{\eta}_b\mathrm{Re}(b_s) - \tilde{\eta}_a\mathrm{Re}(a_s) & -\gamma \\ \tilde{\eta}_a\mathrm{Re}(a_s) - \tilde{\eta}_b\mathrm{Re}(b_s) & \tilde{\eta}_a\mathrm{Im}(a_s) - \tilde{\eta}_b\mathrm{Im}(b_s) & -(\Delta - g\mathrm{om}) \\ \tilde{\eta}_a\mathrm{Im}(\varphi_{-s}) & -\tilde{\eta}_a\mathrm{Re}(\varphi_{-s}) & -\tilde{\eta}_a\mathrm{Im}(\varphi_{+s}) \\ \tilde{\eta}_a\mathrm{Re}(\varphi_{-s}) & \tilde{\eta}_a\mathrm{Im}(\varphi_{-s}) & \tilde{\eta}_a\mathrm{Re}(\varphi_{+s}) \\ -\tilde{\eta}_b\mathrm{Im}(\varphi_{-s}) & -\tilde{\eta}_b\mathrm{Re}(\varphi_{-s}) & \tilde{\eta}_b\mathrm{Im}(\varphi_{+s}) \\ -\tilde{\eta}_b\mathrm{Re}(\varphi_{-s}) & -\tilde{\eta}_b\mathrm{Im}(\varphi_{-s}) & -\tilde{\eta}_b\mathrm{Re}(\varphi_{+s}) \end{bmatrix}$$

$$\begin{bmatrix} \tilde{\eta}_b\mathrm{Re}(b_s) - \tilde{\eta}_a\mathrm{Re}(a_s) & -\tilde{\eta}_a\mathrm{Im}(\varphi_{-s}) & -\tilde{\eta}_a\mathrm{Re}(\varphi_{-s}) & \tilde{\eta}_b\mathrm{Im}(\varphi_{-s}) & \tilde{\eta}_b\mathrm{Re}(\varphi_{-s}) \\ \tilde{\eta}_b\mathrm{Im}(b_s) - \tilde{\eta}_a\mathrm{Im}(a_s) & \tilde{\eta}_a\mathrm{Re}(\varphi_{-s}) & -\tilde{\eta}_a\mathrm{Im}(\varphi_{-s}) & -\tilde{\eta}_b\mathrm{Re}(\varphi_{-s}) & \tilde{\eta}_b\mathrm{Im}(\varphi_{-s}) \\ \Delta - g\mathrm{om} & -\tilde{\eta}_a\mathrm{Im}(\varphi_{+s}) & \tilde{\eta}_a\mathrm{Re}(\varphi_{+s}) & \tilde{\eta}_b\mathrm{Im}(\varphi_{+s}) & -\tilde{\eta}_b\mathrm{Re}(\varphi_{+s}) \\ -\gamma & \tilde{\eta}_a\mathrm{Re}(\varphi_{+s}) & \tilde{\eta}_a\mathrm{Im}(\varphi_{+s}) & -\tilde{\eta}_b\mathrm{Re}(\varphi_{+s}) & -\tilde{\eta}_a\mathrm{Im}(\varphi_{+s}) \\ \tilde{\eta}_a\mathrm{Re}(\varphi_{+s}) & -\gamma_a & \omega_a & 0 & 0 \\ \tilde{\eta}_a\mathrm{Im}(\varphi_{+s}) & -\omega_a & -\gamma_a & 0 & 0 \\ -\tilde{\eta}_b\mathrm{Re}(\varphi_{+s}) & 0 & 0 & -\gamma_b & \omega_b \\ -\tilde{\eta}_b\mathrm{Im}(\varphi_{+s}) & 0 & 0 & -\omega_b & -\gamma_b \end{bmatrix}. \quad (25)$$

The logarithmic negativities EN as a function of detuning for different optomechanical coupling strengths and dissipation rates are shown in Figure 5. Bipartite entanglements of supermode(φ_{+})-supermode(φ_{-}), supermode(φ_{-})-YIG phonon(a), supermode(φ_{-})-membrane phonon(b), and YIG phonon(a)–membrane phonon(b) are mainly present within a finite interval of values of Δ. No entanglement between supermode(φ_{+}) and YIG phonon(a) or between supermode(φ_{+}) and membrane phonon(b) is available, as expected. As shown in Figure 5(a) and (b), when the optomechanical coupling strength equals the magnomechanical coupling strength ($g_{ob} = g_{ma}$), entanglements EN_{s2b}, EN_{s2a}, and EN_{s1s2} increase rapidly. In fact, when g_{ob} is greater (within two orders of magnitude) than or equal to g_{ma}, one can obtain bipartite entanglements in supermode φ_{-}-membrane phonon, supermode φ_{-}-YIG phonon, and YIG phonon-membrane phonon subsystems. When g_{ob} is two orders of magnitude larger than g_{ma}, one can only obtain entanglements of EN_{s1s2} and EN_{s2b} in the system. Moreover, even when the photon–magnon coupling rate is in the weak coupling regime ($\gamma > g_{om}$), we can still obtain bipartite entanglements in these subsystems. For example, Figure 5(b) shows that there are effective bipartite entanglements EN_{s2a} and EN_{s2b} with the photon–magnon

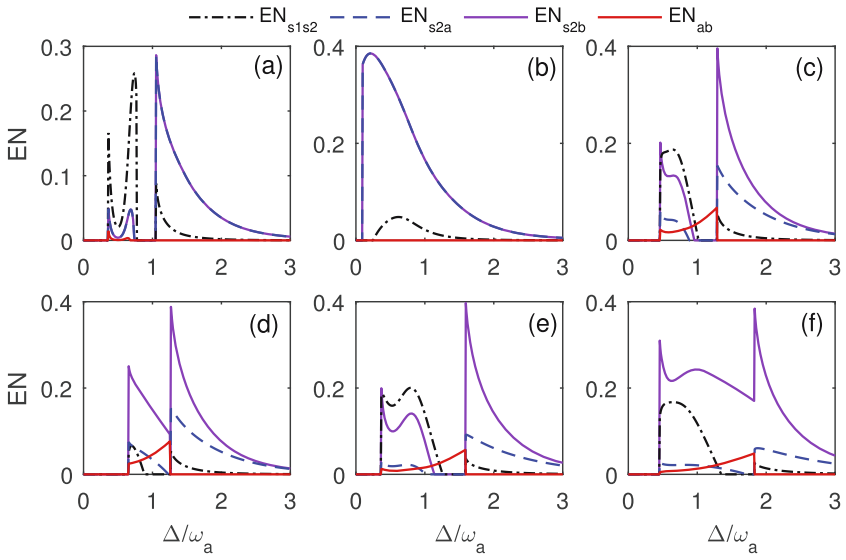

Figure 5: Bipartite entanglements *EN versus* detuning Δ with $g_{ob} = g_{ma}$, $\gamma/2\pi = 1$ MHz in (a), $g_{ob} = g_{ma}$, $\gamma/2\pi = 6$ MHz in (b), $g_{ob} = 2g_{ma}$, $\gamma/2\pi = 3$ MHz in (c), $g_{ob} = 2g_{ma}$, $\gamma/2\pi = 3.5$ MHz in (d), $g_{ob} = 3g_{ma}$, $\gamma/2\pi = 3.5$ MHz in (e) and $g_{ob} = 4g_{ma}$, $\gamma/2\pi = 5$ MHz in (f). The subscript s1 (s2) denotes supermode φ_+ (φ_-). Other parameters are the same as in Figure 2 except for $g_{om} = \omega_a/2$, $T = 0.05$ mK, and $P = 39.5$mW.

coupling rate $g_{om}/2\pi = (\omega_a/2)/2\pi = 5$ MHz and the dissipation rate $\gamma/2\pi = 6$ MHz.

Figure 6 shows the minimum residual contangle $\mathfrak{R}_\tau^{\min}$ of the system with the parameters corresponding to Figure 5. Tripartite entanglements appear in three groups of modes: $\{\varphi_-, a, b\}$, $\{\varphi_+, \varphi_-, b\}$, and $\{\varphi_+, \varphi_-, a\}$, and no tripartite entanglement in $\{\varphi_+, a, b\}$ is found. Figure 6 demonstrates that the tripartite entanglements in the three groups of modes can be adjusted by changing the ratio of g_{ob} to g_{ma}, the dissipation rates κ_m and κ_c, or the detuning Δ. When $g_{ob} = g_{ma}$, the characteristics of the two mechanical modes are almost identical, $\mathfrak{R}_\tau^{\min s1s2a}$ and $\mathfrak{R}_\tau^{\min s1s2b}$ are the same, and the two curves are completely coincident, as shown in Figure 6(a) and (b). When $g_{ob} > g_{ma}$, the tripartite entanglement $\mathfrak{R}_\tau^{\min s1s2b}$ is obviously stronger than $\mathfrak{R}_\tau^{\min s1s2a}$, as shown in Figure 6(c) to (f).

5 Discussion of experimental feasibility

The hybrid magnomechanical and optomechanical cavity system can be implemented using a three-dimensional cavity containing a YIG sphere and a silicon-nitride

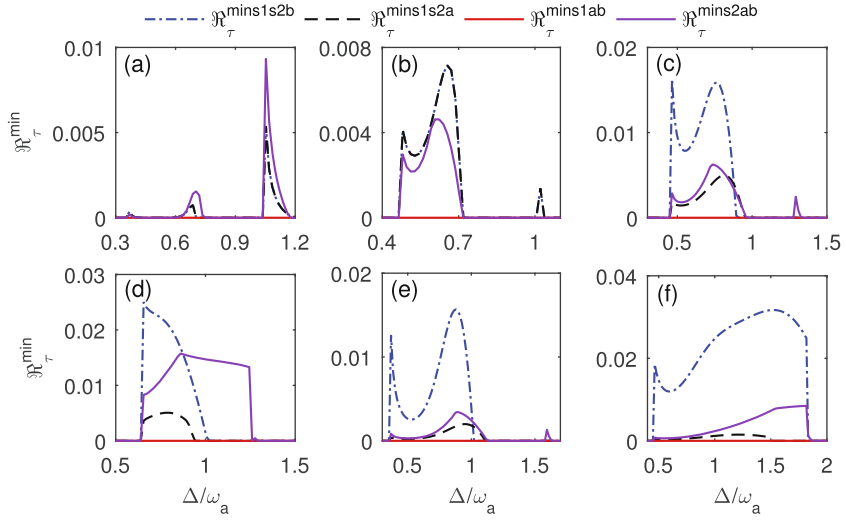

Figure 6: Minimum residual contangle $\mathfrak{R}_\tau^{\min}$ *versus* detuning Δ. The parameters are the same as in Figure 5 except for $\gamma/2\pi = 2$ MHz in (b).

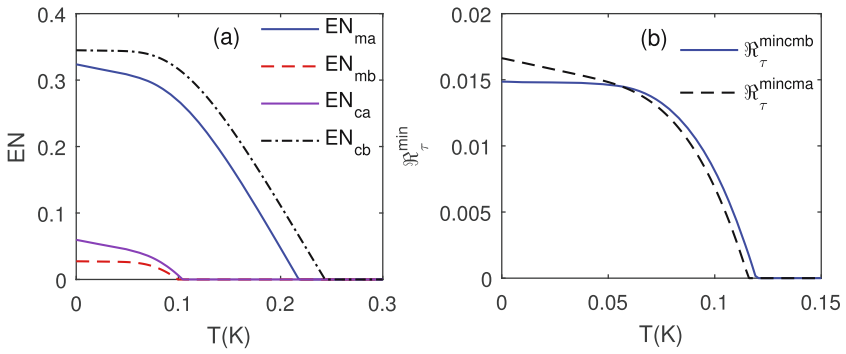

Figure 7: Bipartite entanglements EN_{ma}, EN_{mb}, EN_{ca}, EN_{cb} and tripartite entanglements $\mathfrak{R}_{\tau}^{\text{mincmb}}$, $\mathfrak{R}_{\tau}^{\text{mincma}}$ *versus* T with $g_{om} = 1.4\omega_a$, g_{ob}, κ_m and Δ_m for them are $g_{ob} = [1, 2, 1, 2, 2, 1]g_{ma}$, $\kappa_m = [0.3, 12, 0.3, 12, 12, 0.3]\kappa_c$, $\Delta_m = [2.32, 2.17, 2.32, 2.17, 2.17, 2.32]\omega_a$ respectively. Other parameters are the same as in Figure 2.

membrane [11,16,39,40]. The Kerr term $Km^{\dagger}mm^{\dagger}m$ is ignored in the Hamiltonian, which is caused by the magnetocrystalline anisotropy of YIG sphere with K being the Kerr coefficient. Therefore, the condition $K\,|\langle M\rangle|^3 \ll \Omega_m$ should be met. In fact, the Kerr coefficient ($K = \mu_0 k_{an}\tilde{\gamma}^2/(M^2V)$) is inversely proportional to the volume (V) of the YIG sphere, where k_{an}, $\tilde{\gamma}$, M, and μ_0 are the first-order anisotropy constant, the gyromagnetic ratio, the saturation magnetization, and the vacuum permeability, respectively. For a 1-mm dimeter YIG sphere, the Kerr coefficient is approximately $K/2\pi \approx 10^{-10}$ Hz [11–13]. In the low-lying excitation limit, we obtain $\Omega_m = \sqrt{5N}\tilde{\gamma}B_0/4$ where N is the total spin number of the YIG sphere, $\tilde{\gamma}/2\pi = 28$ GHz/T, $B_0 = \sqrt{2P\mu_0}/(R\sqrt{\pi c})$ with P the driven power, and R the radius of the YIG sphere. The total spin number $N(=\rho V)$ of a 250-μm diameter YIG sphere is about 3.45×10^{16} with the spin density $\rho = 4.22 \times 10^{27}\text{m}^{-3}$. By taking the pump power $P = 17.5$ mW on the 250-μm diameter YIG sphere, we obtain $\Omega_m = 10^{15}$ Hz and $\Omega_m = 1.5 \times 10^{15}$ Hz, with $P = 39.5$ mW. For the parameters in the above figures, the value of $|\langle M\rangle|$ falls within the range of 3.5×10^6 to 1.27×10^7. Thus, for a 250-μm diameter YIG sphere, $K/2\pi \approx 6.4 \times 10^{-9}$ Hz, $K\,|\langle m\rangle|^3 \le 8.24 \times 10^{13} \ll \Omega_m$. The condition of low-lying excitations, $\langle m^{\dagger}m\rangle \ll 5N$, is also well satisfied.

When the magnetic dipole interaction between the cavity mode and the magnon mode is larger than the frequency of the mechanical oscillator, it is easy to obtain bipartite entanglements EN_{ma}, EN_{mb}, EN_{ca}, and EN_{cb}. These entanglements still survive when the temperature reaches 100 mk, as shown in Figure 7. The tripartite entanglements $\mathfrak{R}_{\tau}^{\text{mincmb}}$ and $\mathfrak{R}_{\tau}^{\text{mincma}}$ are also effective at

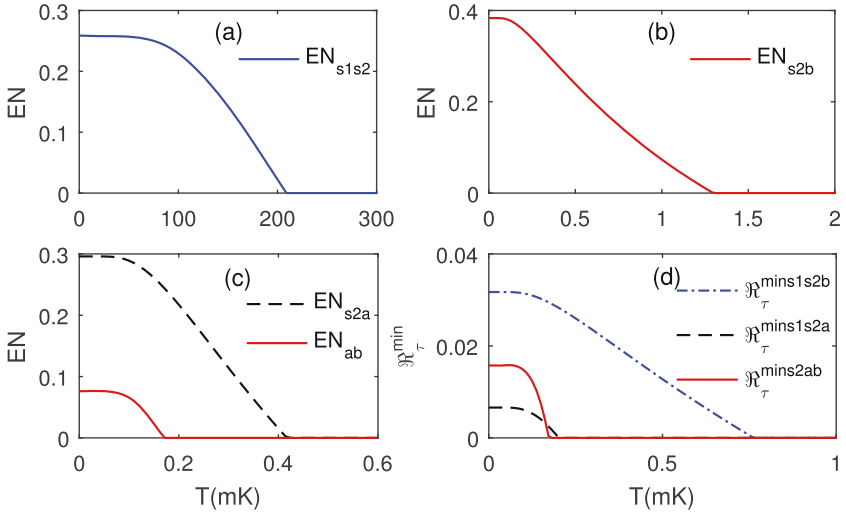

Figure 8: Bipartite and tripartite entanglements *versus* T. g_{ob}, κ_m and Δ for EN_{s1s2}, EN_{s2b}, EN_{s2a}, EN_{ab}, $\mathfrak{R}_{\tau}^{\text{minsls2b}}$, $\mathfrak{R}_{\tau}^{\text{minsls2a}}$, $\mathfrak{R}_{\tau}^{\text{minsls2ab}}$ are $g_{ob} = [1, 2, 1, 2, 4, 1, 2]g_{ma}$, $\gamma/2\pi = [1, 3.5, 1, 3.5, 5, 1, 3.5]$ MHz, $\Delta = [0.74, 1.27, 1.05, 1.25, 1.52, 1.05, 0.86]\omega_a$. Other parameters are the same as in Figure 5.

temperatures higher than 100 mK. Moreover, when the temperature reaches 100 mK, the entanglement and entanglement transfer effects in Figures 2 and 4 change little and remain very well. By introducing the supermodes formed by the cavity mode and the magnon mode, the entanglement between the two mechanical oscillators can be obtained under the condition that the optomechanical interaction strength is equal to or slightly larger than the magnomechanical coupling strength ($g_{ma} \leq g_{ob} \leq 10g_{ma}$). When g_{ob} is two orders of magnitude larger than g_{ma}, there are only effective EN_{s1s2} and EN_{s2b} left in the system. The drawback is that the entanglement related to the mechanical oscillator in the system is very sensitive to thermal noise. Under the condition of $g_{om} < \omega_a$, obtaining entanglements in the system has strict requirements on temperature. As shown in Figure 8, the entanglement between the two supermodes is robust to temperature and can exist in an environment with temperatures higher than 200 mK. However, effective EN_{s2a}, EN_{ab}, and tripartite entanglements in the system only exist with temperatures lower than 1 mK.

6 Conclusion

In summary, we have investigated in detail the bipartite and tripartite stationary continuous-variable entanglements in a hybrid cavity system containing a YIG sphere and membrane mechanical oscillator. Stationary magnon–YIG phonon entanglement and photon–membrane phonon entanglement are established owing to the magnetostrictive interaction and the optomechanical interaction. With experimentally reachable parameters, these initial entanglements can be transferred to magnon–membrane phonon and photon-YIG phonon entanglements. The system also exhibits genuine tripartite photon–magnon–YIG phonon and photon–magnon–membrane phonon entanglements. One can easily switch between these tripartite entanglements by adjusting the detuning. By introducing the supermodes formed by the cavity mode and magnon mode, the two mechanical modes interact with the supermodes simultaneously, and the entanglement between the two mechanical oscillators can be obtained under the condition that the optomechanical interaction strength is equal to or slightly larger than the magnomechanical coupling strength. Our scheme could provide a potential role for bipartite and tripartite entanglements transfer among different modes in hybrid physical platforms.

Acknowledgments: The authors are grateful for the reviewer's valuable comments that improved the manuscript.

Funding information: This work is supported by the project of the National Natural Science Foundation of China [Grant Number 62062035] and the project of the Education Bureau of Jiangxi Province [Grant Number GJJ200645].

Author contributions: LMC contributed the central idea and wrote the initial draft of the paper. The remaining authors contributed to refining the ideas, carrying out additional analyses and finalizing this paper. All authors have accepted responsibility for the entire content of this manuscript and approved its submission.

Conflict of interest: The authors state no conflict of interest.

Data availability statement: The datasets generated during the current study are available from the corresponding author on reasonable request.

References

[1] Chumak AV, Vasyuchka VI, Serga AA, Hillebrands B. Magnon spintronics. Nat Phys. 2015;11(6):453–61.
[2] Serga AA, Chumak AV, Hillebrands B. YIG magnonics. J Phys D Appl Phys. 2010;43(26):264002.
[3] Kong C, Bao XM, Liu JB, Xiong H. Magnon-mediated nonreciprocal microwave transmission based on quantum interference. Opt Express. 2021;29(16):25477.
[4] Zhang X, Zou CL, Jiang L, Tang HX. Strongly coupled magnons and cavity microwave photons. Phys Rev Lett. 2014;113(15):156401.
[5] Tabuchi Y, Ishino S, Ishikawa T, Yamazaki R, Usami K, Nakamura Y. Hybridizing ferromagnetic magnons and microwave photons in the quantum limit. Phys Rev Lett. 2014;113(8):083603.
[6] Zhang D, Wang XM, Li TF, Luo XQ, Wu W, Nori F, et al. Cavity quantum electrodynamics with ferromagnetic magnons in a small yttrium-iron-garnet sphere. NPJ Quantum Inf. 2015;1(1):15014.
[7] Bourhill J, Kostylev N, Goryachev M, Creedon DL, Tobar ME. Ultrahigh cooperativity interactions between magnons and resonant photons in a YIG sphere. Phys Rev B. 2016;93(14):144420.
[8] Xu J, Zhong C, Han X, Jin D, Jiang L, Zhang X. Floquet cavity electromagnonics. Phys Rev Lett. 2020;125(23):237201.
[9] Rao JW, Wang YP, Yang Y, Yu T, Gui YS, Fan XL, et al. Interactions between a magnon mode and a cavity photon

mode mediated by traveling photons. Phys Rev B. 2020;101(6):064404.
[10] Aspelmeyer M, Kippenberg TJ, Marquardt F. Cavity optomechanics. Rev Mod Phys. 2014;86(4):1391.
[11] Zhang X, Zou CL, Jiang L, Tang HX. Cavity magnomechanics. Sci Adv. 2016;2:e1501286.
[12] Wang YP, Zhang GQ, Zhang D, Luo XQ, Xiong W, Wang SP, et al. Magnon Kerr effect in a strongly coupled cavity-magnon system. Phys Rev B. 2016;94(22):224410.
[13] Zhang GQ, Wang YP, You JQ. Theory of the magnon Kerr effect in cavity magnonics. Sci China-Phys Mech Astron. 2019;62(8):987511.
[14] Wang YP, Zhang GQ, Zhang D, Li TF, Hu CM, You JQ. Bistability of cavity magnon polaritons. Phys Rev Lett. 2018;120(5):057202.
[15] Kong C, Xiong H, Wu Y. Magnon-induced nonreciprocity based on the magnon Kerr effect. Phys Rev Appl. 2019;12(3):034001.
[16] Liu ZX, Xiong H, Wu Y. Magnon blockade in a hybrid ferromagnet-superconductor quantum system. Phys Rev B. 2019;100(13):134421.
[17] Xie JK, Ma SL, Li FL. Quantum-interference-enhanced magnon blockade in an yttrium-iron-garnet sphere coupled to superconducting circuits. Phys Rev A. 2020;101(4):042331.
[18] Zhao C, Li X, Chao S, Peng R, Li C, Zhou L. Simultaneous blockade of a photon, phonon, and magnon induced by a two-level atom. Phys Rev A. 2020;101(6):063838.
[19] Wang L, Yang ZX, Liu YM, Bai CH, Wang DY, Zhang S, et al. Magnon blockade in a PT-Řsymmetric-Řlike cavity magnomechanical system. Ann Phys (Berlin). 2020;532(7):2000028.
[20] Haghshenasfard Z, Cottam MG. Sub-Poissonian statistics and squeezing of magnons due to the Kerr effect in a hybrid coupled cavity-magnon system. J Appl Phys. 2020;128(3):033901.
[21] Horodecki R, Horodecki P, Horodecki M, Horodecki K. Quantum entanglement. Rev Mod Phys. 2009;81:865.
[22] Vitali D, Gigan S, Ferreira A, Böhm HR, Tombesi P, Guerreiro A, et al. Optomechanical entanglement between a movable mirror and a cavity field. Phys Rev Lett. 2007;98(3):030405.
[23] Sete EA, Eleuch H, Raymond Ooi CH. Entanglement between exciton and mechanical modes via dissipation-induced coupling. Phys Rev A. 2015;92(3):033843.
[24] Ockeloen-Korppi CF, Damskägg E, Pirkkalainen JM, Asjad M, Clerk AA, Massel F, et al. Stabilized entanglement of massive mechanical oscillators. Nature. 2018;556(7702):478–82.
[25] Zhang Z, Scully MO, Agarwal GS. Quantum entanglement between two magnon modes via Kerr nonlinearity driven far from equilibrium. Phys Rev Res. 2019;1:023021.
[26] Yang ZB, Liu JS, Jin H, Zhu QH, Zhu AD, Liu HY, et al. Entanglement enhanced by Kerr nonlinearity in a cavity-optomagnonics system. Opt Express. 2020;28(21):31862–71.
[27] Nair JMP, Agarwal GS. Deterministic quantum entanglement between macroscopic ferrite samples. Appl Phys Lett. 2020;117:084001.
[28] Kong D, Hu X, Hu L, Xu J. Magnon-atom interaction via dispersive cavities: magnon entanglement. Phys Rev B. 2021;103:224416.
[29] Li J, Zhu SY, Agarwal GS. Magnon-photon-phonon entanglement in cavity magnomechanics. Phys Rev Lett. 2018;121(20):203601.
[30] Bai CH, Wang DY, Wang HF, Zhu AD, Zhang S. Robust entanglement between a movable mirror and atomic ensemble and entanglement transfer in coupled optomechanical system. Sci Rep. 2016;6:33404.
[31] Zhang Q, Zhang X, Liu L. Transfer and preservation of entanglement in a hybrid optomechanical system. Phys Rev A. 2017;96:042320.
[32] Mu Q, Li H, Huang X, Zhao X. Microscopic-macroscopic entanglement transfer in optomechanical system: non-Markovian effects. Opt Commun. 2018;426:70–6.
[33] Chen YT, Du L, Zhang Y, Wu JH. Perfect transfer of enhanced entanglement and asymmetric steering in a cavity-magnomechanical system. Phys Rev A. 2021;103:053712.
[34] Cai Q, Liao J, Shen B, Guo G, Zhou Q. Microwave quantum illumination via cavity magnonics. Phys Rev A. 2021;103:052419.
[35] Vidal G, Werner RF. Computable measure of entanglement. Phys Rev A. 2002;65(3):032314.
[36] Adesso G, Serafini A, Illuminati F. Extremal entanglement and mixedness in continuous variable systems. Phys Rev A. 2004;70(2):022318.
[37] Adesso G, Illuminati F. Continuous variable tangle, monogamy inequality, and entanglement sharing in Gaussian states of continuous variable systems. New J Phys. 2006;8:15.
[38] Xu Y, Liu JY, Liu WJ, Xiao YF. Nonreciprocal phonon laser in a spinning microwave magnomechanical system. Phys Rev A. 2021;103:053501.
[39] Tabuchi Y, Ishino S, Noguchi A, Ishikawa T, Yamazaki R, Usami K, et al. Coherent coupling between a ferromagnetic magnon and a superconducting qubit. Science. 2015;349:405.
[40] Liu YL, Liu QC, Wang SP, Chen Z, Sillanpaa MA, Li TF. Optomechanical anti-lasing with infinite group delay at a phase singularity. Phys Rev Lett. 2021;127(27):273603.